



**HAL**  
open science

## Artificial neural network modeling of cefixime photodegradation by synthesized CoBi(2)O(4) nanoparticles

Oussama Baaloudj, Nouredine Nasrallah, Mohamed Kebir, Bouzid Guedioura, Abdeltif Amrane, Phuong Nguyen-Tri, Sonil Nanda, Aymen Amin Assadi

### ► To cite this version:

Oussama Baaloudj, Nouredine Nasrallah, Mohamed Kebir, Bouzid Guedioura, Abdeltif Amrane, et al.. Artificial neural network modeling of cefixime photodegradation by synthesized CoBi(2)O(4) nanoparticles. Environmental Science and Pollution Research, 2021, 28 (12), pp.15436-15452. 10.1007/s11356-020-11716-w . hal-03037964

**HAL Id: hal-03037964**

**<https://hal.science/hal-03037964v1>**

Submitted on 19 May 2021

**HAL** is a multi-disciplinary open access archive for the deposit and dissemination of scientific research documents, whether they are published or not. The documents may come from teaching and research institutions in France or abroad, or from public or private research centers.

L'archive ouverte pluridisciplinaire **HAL**, est destinée au dépôt et à la diffusion de documents scientifiques de niveau recherche, publiés ou non, émanant des établissements d'enseignement et de recherche français ou étrangers, des laboratoires publics ou privés.

1                   **Artificial neural network modeling of Cefixime photodegradation by**  
2                   **synthesized CoBi<sub>2</sub>O<sub>4</sub> nanoparticles**

3                   Oussama Baaloudj<sup>a</sup>, Nouredine Nasrallah<sup>a</sup>, Mohamed Kebir<sup>a,b</sup>, Bouzid  
4                   Guedioura<sup>c</sup>, Abdeltif Amrane<sup>d</sup>, Phuong Nguyen-Tri<sup>e\*</sup>, Sonil Nanda<sup>f</sup>, Aymen Amin  
5                   Assadi<sup>d\*</sup>

6                   <sup>a</sup>Laboratory of Reaction Engineering, Faculty of Mechanical Engineering and Process Engineering  
7                   USTHB, BP 32, Algiers, Algeria

8                   <sup>b</sup> Research Unit on Analysis and Technological Development in Environment (URADTE-CRAPC), BP  
9                   384, Bou-Ismaïl Tipaza, Algeria

10                   <sup>c</sup> Reactor division, Nuclear Research Center, Draria, Algeria

11                   <sup>d</sup> Univ Rennes - ENSCR / UMR CNRS 6226 "Chemical Sciences of Rennes" ENSCR, Campus de  
12                   Beaulieu, av. du Général Leclerc, 35700 Rennes, France

13                   <sup>e</sup> Université du Québec à Trois-Rivières (UQTR), Trois-Rivières, Québec, G9A 5H7, Canada

14                   <sup>f</sup>Department of Chemical and Biological Engineering, University of Saskatchewan, Saskatoon,  
15                   Saskatchewan, S7N 5A9, Canada

16  
17                   \* Corresponding authors: E-mail: [aymen.assadi@ensc-rennes.fr](mailto:aymen.assadi@ensc-rennes.fr) (A. A. Assadi); Tel.: +33 223238152  
18                   [Phuong.Nguyen-Tri@uqtr.ca](mailto:Phuong.Nguyen-Tri@uqtr.ca) (P. Nguyen-Tri); Tel : + 819 376-5011  
19

20                   **Abstract**

21                   CoBi<sub>2</sub>O<sub>4</sub> (CBO) nanoparticles were synthesized by sol-gel method using  
22                   Polyvinylpyrrolidone (PVP) as a complexing reagent. For a single-phase with the spinel  
23                   structure, the formed gel was dried and calcined at four temperatures stages. Various  
24                   methods were used to identified and characterized the obtained spinel, such as X-ray  
25                   diffraction (XRD), Scanning Electron Micrograph (SEM-EDX), Transmission electron  
26                   microscope (TEM), Fourier transform infrared (FT-IR), X-ray fluorescence (XRF),  
27                   Raman and UV-Vis spectroscopies. The photocatalytic activity of CBO was examined  
28                   for the degradation of a pharmaceutical product Cefixime (CFX). Furthermore, for the  
29                   prediction of the CFX degradation rate an artificial neural network model was used.  
30                   The network was trained using the experimental data obtained at different pH with  
31                   different CBO doses and initial CFX concentrations. To optimize the network, various  
32                   algorithms and transfer functions for the hidden layer were tested. By calculating the

33 mean square error (MSE), 13 neurons were found to be the optimal number of neurons  
34 and produced the highest coefficient of correlation  $R^2$  of 99.6 %. The relative  
35 significance of the input variables was calculated and the most impacting input was  
36 proved to be the initial CFX concentration. The effects of some scavenging agents  
37 were also studied. The results confirmed the dominant role of hydroxyl radical  $\text{OH}^\bullet$  in  
38 the degradation process. With the novel  $\text{CoBi}_2\text{O}_4/\text{ZnO}$  hetero-system, the  
39 photocatalytic performance has been enhanced, giving an 80% degradation yield of  
40 CFX (10 mg/L) at neutral pH in only 3 hours.

41 **Keywords:**  $\text{CoBi}_2\text{O}_4$  Spinel, Characterization, Cefixime, Artificial neural network,  
42 Optimization.

### 43 1. Introduction

44 In recent years, pharmaceutical compounds have sullied the aqueous environment,  
45 among those compounds, antibiotics are the major concern which are extremely  
46 dangerous because they are widely used in both human and veterinary medicines  
47 (Kaczala and E. Blum 2015). Antibiotics are also used to improve feed quality and thus  
48 increase rates in the poultry industries (World Health Organisation 2011). Analytical  
49 study of antibiotic use in 76 countries from 2010-2015 found that global antibiotic  
50 consumption has increased by 65% for the fifteen years studied (Sample 2018). The  
51 majority of antibiotic products are not biodegradable and their environmental  
52 contamination can increase aquatic toxicity (Mostafaloo et al. 2019). Generally,  
53 antibiotics are present at amounts ranging from ng/L to  $\mu\text{g/L}$  in treated wastewater  
54 (Ibáñez et al. 2017; Shokoohi et al. 2017; Mirzaei et al. 2018). But even in small  
55 amounts, the presence of these compounds in water supplies will increase bacterial  
56 resistance, which produces a kind of micro-organisms called superbugs or antibiotic  
57 resistance (ABR) that are considered to cause very dangerous health effects (Elder et  
58 al. 2020). ABR is the ability to survive and multiply in the presence of antibiotic doses  
59 that are eventually deemed effective against a bacterial population or other  
60 microorganisms (Elder et al. 2020). A statistics study indicates that antibiotic resistance  
61 causes 700,000 deaths globally each year (Liu et al. 2019). ABR is now, in the 21st  
62 century, widely recognized as a grave threat to global health ~~in the 21st century~~  
63 (Littmann et al. 2015).

64 As a typical example of antibiotics, Cefixime (CFX) was chosen which belonging to  
65 broad-spectrum, third-generation cephalosporin antibiotic derived semi-synthetically  
66 from the marine fungus *Cephalosporium acremonium* (Shooshtari and Ghazi 2017).  
67 CFX with molecular formula  $C_{16}H_{15}N_5O_7S_2$  (Fig. 1) is (6R,7R)-7-[[[(2Z)-2-(2-amino -1,3-  
68 thiazol -4- yl) -2- (carboxymethoxyimino) acetyl] amino] -3- ethenyl -8- oxo -5- thia -1-  
69 azabicyclo [4.2.0] oct-2-ene-2-carboxylic acid (Sheydaei et al. 2018). A study detected  
70 CFX as one of the most prevalent antibiotics observed in different water environments  
71 with concentrations of 278.65 to 422.1 ng/L (Mirzaei et al. 2018).

72 *Fig. 1 Molecular structure of the antibiotic Cefixime.*

73 Most of the conventional approaches that are commonly used for the removal of  
74 antibiotics have no positive findings for the degradation of antibiotic residues from  
75 contaminated waters or have substantial inconveniences such as by-products of the  
76 degradation (Xiong et al. 2018; Zhu et al. 2018; Zhang et al. 2020). On the other hand,  
77 Advanced Oxidation Processes (AOPs) have proven to be an effective solution for the  
78 rapid degradation of non-biodegradable substances in polluted water (Lou et al. 2017;  
79 Aboudalle et al. 2018; Kamagate et al. 2018). Particularly, the Heterogeneous  
80 photocatalysis process which is one of the best approaches for aqueous environment  
81 treatment as it is safer and a natural technology (used green energy). photocatalysis  
82 has proven on a previous investigations a successful degradation for various types of  
83 pharmaceutical drugs and organic compounds in the wastewater (Kamagate et al.  
84 2018; Nguyen et al. 2018; Li et al. 2019b; Sayadi et al. 2019). Photocatalysis is based  
85 generally on the principle of the activation of a catalyst using an energy provided by a  
86 source of light (Homem and Santos 2011). As a catalyst, semiconductors are  
87 commonly used as they are very effective and easy to synthesize. Recently, many  
88 bismuth-based semiconductors have become very significant because of their high  
89 chemical stability, their excellent ability to absorb light and its narrow optical band gap  
90 (Tho et al. 2020). Cobalt bismuthate with the chemicals formula  $CoBi_2O_4$  (CBO) was  
91 chosen as a typical semiconductor. To our knowledge, only one study has dealt with  
92 the synthesis and use of CBO photocatalyst (Jagadeesh and Sailaja 2019). Moreover,  
93 no study has been made yet concerning  $CoBi_2O_4/ZnO$  hetero-system.

94 Artificial neural network (ANN) is one of the most powerful tools for modeling linear  
95 and non-linear systems (Mohammadzadeh Kakhki et al. 2020). It an effective way of  
96 predicting experimental patterns in various systems, especially for photocatalysis

97 (Zhou et al. 2020) Moreover, ANN has the self-learning ability and to work with  
98 incomplete knowledge, storing information on the entire network, having fault tolerance  
99 and a distributed memory (Kaur and Kaur 2014). Thus, modeling and optimization can  
100 be accomplished without the rigor of the experimental information via ANN (Ayodele et  
101 al. 2020). Owing to that, ANN has been employed in the prediction of photocatalysis  
102 CFX efficiency. The challenge in the ANN modeling is to build a network with the  
103 smallest possible number of random experimental points to modulate and achieve the  
104 expected results approach to real cases without designing an experimental model.  
105 Only a few studies have attempted this challenge (Hassani et al. 2015; Tabatabai-  
106 Yazdi et al. 2019; Zulfiqar et al. 2019). To find the most efficient and effective network,  
107 various algorithms and transfer functions for the hidden layer has been attempted.

108 In this study, we report the synthesis of  $\text{CoBi}_2\text{O}_4$  nanoparticles which prepared by  
109 sol-gel auto combustion method using polyvinylpyrrolidone (PVP) as a complexing  
110 reagent. Various methods were used to identified and characterized the obtained  
111 spinel, such as XRD, SEM-EDX, TEM, FT-IR, XRF, Raman and UV-Vis  
112 spectroscopies. After that, Cefixime was considered as a model of antibiotic compound  
113 to tested the photocatalytic performance of this catalyst. The effect of pH, irradiation  
114 time, the concentration of CFX and concentration of catalyst on the degradation of CFX  
115 was examined and modeled using ANN. Also, a Garson formula was introduced to  
116 measure the relative significance of different input variables. After that, the effects of  
117 some scavenging agents have been studied. Finally, the new hetero-system  
118  $\text{CoBi}_2\text{O}_4/\text{ZnO}$  has been tested in order to enhance the photocatalytic performance.

## 119 **2. Material and methods**

### 120 **2.1 Chemicals**

121 Chemicals used in the present study were bismuth nitrate pentahydrate  
122  $[\text{Bi}(\text{NO}_3)_3 \cdot 5\text{H}_2\text{O}]$  (98.5% Chem-Lab), cobalt nitrate hexahydrate  $[\text{Co}(\text{NO}_3)_2 \cdot 6\text{H}_2\text{O}]$  (98%  
123 Biochem), Zinc nitrate hexahydrate  $[\text{N}_2\text{O}_6\text{Zn} \cdot 6\text{H}_2\text{O}]$  (98% Biochem), Cefixime  
124 trihydrate and Polyvinylpyrrolidone were obtained from a pharmaceutical company  
125 Pharmalliance Algeria, ethanol from Biochem, Sodium hydroxide, Hydrochloric acid,  
126 isopropanol and nitric acid were supplied by Sigma Aldrich. All chemicals were used  
127 as received without further purification. Distilled water has been used as a solvent.

## 128 2.2 Synthesis of CoBi<sub>2</sub>O<sub>4</sub> nanoparticles

129 CoBi<sub>2</sub>O<sub>4</sub> was synthesized by the aqueous PVP sol-gel method. The gel was  
130 prepared using stoichiometric amounts (1:2 ratio) of cobalt nitrate hexahydrate  
131 [Co(NO<sub>3</sub>)<sub>2</sub>·6H<sub>2</sub>O] and bismuth nitrate pentahydrate [Bi(NO<sub>3</sub>)<sub>3</sub>·5H<sub>2</sub>O] respectively. They  
132 were then dissolved in ethanol by using a magnetic stirrer; an excess of 5% citric acid  
133 was added in the solutions. After total solubilization, both solutions had been mixed  
134 and heated at 50 °C for 1h.

135 In the following step, Polyvinylpyrrolidone (PVP K30), used as a complexing  
136 agent was dissolved in 50 mL water and added to the reaction solution, applied about  
137 15% w/w to obtain the complexing role (Giannopoulou et al. 2015). After concentrating  
138 the solutions by evaporation at 80 °C under stirring, the mixed solution turned into a  
139 reddish transparent gel. After drying and combustion at 200 °C for 6 h a precursor gel  
140 powder was formed (Xerogel).

141 The amorphous powder was subjected to calcination at 300°C, 400°C, 600°C and  
142 800°C in an air oven each one for 3 h. The synthesized sample was annealed to  
143 improve the degree of crystallinity and to eliminate any leftover carbonated waste after  
144 the combustion reaction. Then, it was subjected to phase identification, microstructural  
145 analysis and photocatalytic studies.

## 146 2.3 Characterization

147 The XRD analysis of the products was recorded by a Phillips PW 1730, X-ray  
148 diffractometer using monochromatized Cu K radiation ( $\lambda = 0.15417$  nm the morphology  
149 of the sample SEM was studied using the electron scanning microscope FEI Quanta  
150 650 equipped with EDX and Mapping analysis with 20 kV accelerated voltage.  
151 Transmission electron microscope (TEM) images of the nanostructures were taken on  
152 a JEOL-24011BU. ATR-FTIR spectra were obtained in the range of 400–4000 cm<sup>-1</sup>  
153 with an Alpha Bruker spectrometer (One FTIR model). The chemical analysis was  
154 carried out by using Xray fluorescence (PANalytical epsilon3-XL spectrometer). UV–  
155 visible diffuse reflectance spectrum (DRS) of the sample was produced by dry pressed  
156 disk sample using Cary 5000 UV–vis. The Raman analysis was carried out using  
157 LabRAM HR Evolution system Horiba Jobin-Yvon.

158 2.4 Photocatalytic degradation study

159 We selected (CFX) as a pharmaceutical model contaminant to investigate  
160 CoBi<sub>2</sub>O<sub>4</sub>'s photocatalytic performance. The photocatalytic degradation of CFX was  
161 conducted by mixing an appropriate quantity of CoBi<sub>2</sub>O<sub>4</sub> in 100 mL of CFX solution  
162 with known concentration. The pH was set to the desired value with NaOH and HCl.  
163 The solution was continuously stirred for 2h in dark conditions in a closed reactor to  
164 reach the balance of adsorption and desorption before switching on the light. As a  
165 visible light source, a tungsten bulb 200 W manufactured by Osram was applied and  
166 positioned at 10 cm from the solution surface. The intensity (8.25 mW/cm<sup>2</sup>) and the  
167 maximum emission (630 nm) of the lamp were measured by a digital flux meter (Testo  
168 545). A cooling system consisting of a double-walled reactor attached to a thermostatic  
169 bath (Daihan Labtech, LCB-11D) has been used to maintain the temperature of the  
170 solution nearly constant (25 ± 1 °C) during the photocatalytic experiments. At a regular  
171 time, 2 mL of the solution was centrifuged at the speed of 5,000 rpm for 10 min to filter  
172 the suspended CoBi<sub>2</sub>O<sub>4</sub> particles from the sample and directly analyzed by UV-Visible  
173 spectrometry (OPTIZEN, UV-3220UV) at the maximum absorption wavelength of CFX  
174 (288 nm). It should be mentioned that the small positive error of UV-Visible  
175 spectrometry in comparison with HPLC was ignored. The following equation was used  
176 to calculate the degradation rate of CFX.

$$Photodegradation\% = \frac{(C_o - C)}{C_o} \times 100 \quad (1)$$

177 Where C<sub>o</sub> is the initial concentration of CFX after adsorption and C is the  
178 concentration of CFX at time t.

179 As already mentioned, the CFX concentration was monitored by measuring the  
180 absorbance of the samples using a UV–Visible spectrophotometry. The degradation of  
181 the pollutant was followed by the disappearance of the band corresponding to CFX at  
182 288 nm as shown in figure 2. The experiment was conducted in the presence of 0.1 g  
183 CBO at pH 6, room temperature and an initial CFX concentration of 10 mg/L.

184 To evaluate the CFX mineralization by the catalyst CBO, the amount of total  
185 organic carbon (TOC) in the solution at a regular time with the same conditions was  
186 measured by TOC analyzer (Shimadzu TOC-L, Japan) using the catalytic combustion

187 method at 680°C. The results of TOC analysis are presented in Fig. 2 (b). The following  
188 equation was used to calculate the TOC removal (%):

$$TOC_{removal}\% = \frac{(TOC_o - TOC)}{TOC_o} \times 100 \quad (2)$$

189 where  $TOC_o$  (mg) is the initial TOC values after adsorption,  $TOC$  (mg) is the remaining  
190 TOC in solution.

191 the TOC removal reached 67.23% in the presence of CBO catalyst after 6 h, which  
192 confirmed that cefixime could be effectively mineralized in the presence of CBO  
193 photocatalyst under visible light irradiation.

194 *Fig. 2 (a) UV-visible spectra (B)TOC removal of CFX (10 mg/L).*

## 195 2.5 Experimental design and modeling

196 The input layer consisted of four numbers of neurons, which are pH, irradiation  
197 time (min), the dose of CBO (g/L) and concentration of CFX (mg/L), while  
198 photodegradation of CFX (%) was selected as the output layer. The application was  
199 performed in the laboratory to obtain the actual responses. As it is a challenge to build  
200 a network with the smallest possible number of random experimental points to  
201 approach to real cases without designing an experimental model. For that, a total of  
202 40 random experimental points has been randomly divided into 70% training, 15%  
203 testing and 15% validation data. Training data were presented to the network during  
204 training. The use of validation data was to test network generalization and to stop  
205 training if generalization stops. The test data provided a fully independent network  
206 performance measurement during and following training (Ayoubi-Feiz et al. 2019).

207 The modeling of the photodegradation of CFX was carried out by MATLAB  
208 R2014a which has been widely used (Medarević et al. 2016; Ayoubi-Feiz et al. 2019;  
209 Tabatabai-Yazdi et al. 2019; Zulfiqar et al. 2019; Garg et al. 2020). The model  
210 parameters are described in Table 1. For the model development, the feed-forward  
211 neural network with backpropagation method was used. Furthermore, a supervised  
212 learning technique called Levenberg-Marquardt with a training function 'trainlim' has  
213 been used for training the network.

214 *Table 1 ANN model parameters.*



215 The number of hidden neurons is a critical element of modeling experimental  
 216 processes with ANN (Hazrati et al. 2017). For its optimization, a set of topologies have  
 217 been used in which the number of hidden neurons changed from 2 to 20. The mean  
 218 square error MSE was performed to investigate the relation between the hidden  
 219 neurons and the network error (Ayoubi-Feiz et al. 2019). The MSE function was used  
 220 as Eq.3. The coefficient of correlation R (Eq.4) used to predict model conformity and  
 221 applicability, the more the value is close to one, the better it is applied.

$$MSE = \frac{1}{n} \sum_{i=1}^n (y_{i,NN} - y_{i,exp})^2 \quad (3)$$

$$R^2 = 1 - \frac{\sum_{i=1}^n (y_{i,NN} - y_{i,exp})^2}{\sum_{i=1}^n (y_m - y_{i,exp})^2} \quad (4)$$

222 where  $n$  is the total number of data points,  $y_{i,NN}$  and  $y_{i,exp}$  are the network prediction  
 223 and the experimental response and  $i$  is an index of the data,  $y_m$  is the average of the  
 224 actual values.

### 225 3. Results and discussion

#### 226 3.1 Characterization of the catalyst

227 To confirm the single phase of  $\text{CoBi}_2\text{O}_4$ , an X-ray diffraction (XRD) pattern after  
 228 each calcination was taken. Figure 3 illustrates the effect of different annealing  
 229 temperatures on the structure of the synthesized samples. The pure  $\text{CoBi}_2\text{O}_4$  nano-  
 230 powders were obtained at 800 °C (after annealing at 300 °C, 400 °C, 600 °C) almost  
 231 a single phase of CBO without impurity was observed. The phase of the  $\text{CoBi}_2\text{O}_4$  could  
 232 be indexed with the five main diffraction peaks at  $2\theta = 27.88^\circ$  (111),  $33.12^\circ$  (200),  
 233  $45.72^\circ$  (220),  $52.76^\circ$  (311) and  $56.04^\circ$  (222) which were in good agreement with the  
 234 reference peaks (Jagadeesh and Sailaja 2019) almost the same, and also in line with  
 235 the standard card (JCPDS 50-0369) from Joint Committee of Powder Diffraction  
 236 Standards of the face-centered cubic of  $\text{CoBi}_2\text{O}_4$ .

237 The crystallite size was calculated from the main diffraction peaks of the last  
 238 calcined product (at 800 °C) with the following Debye- Scherer formula Eq. (5). The  
 239 crystalline sizes have been estimated between 19.45 and 46.39 nm.

$$D = \frac{K\lambda}{\beta \cos(\theta)} \quad (5)$$

240 where D is the crystallite size of the phase-in nanometers, K is the Scherrer constant.  
241 ( $K = 0.94$  for cubic symmetry),  $\lambda$  is the wavelength of the X-ray beam used,  $\beta$  is the full  
242 width at half maxima (FWHM) in radians and  $\theta$  is the Braggs angle.

243 *Fig. 3 XRD diffractogram of  $\text{CoBi}_2\text{O}_4$  calcined at (a) 300°C, (b) 400°C, (c) 600°C and*  
244 *(d) 800°C.*

245 For the XRD patterns of the ZnO nanoparticles prepared via co-precipitation. As  
246 shown in Figure 4, the ZnO nanoparticles displayed a Wurtzite structure (hexagonal  
247 phase, space group P63mc). All standard peaks observed for ZnO nanoparticles were  
248 in line with those obtained from (JCPDS 36-1451) (Raou 2017).

249 *Fig. 4 XRD diffractogram of ZnO.*

250 The spinel structure may be considered as a continuously bound crystal in which  
251 the atoms are bonded by equivalent forces (ionic, covalent or van der Waals) to all  
252 nearest neighbors. The spinel shaped metal ions are found in two separate sub-lattices  
253 known as A-site (tetrahedral) and B-site (octahedral), as stated in the geometric  
254 arrangement of the nearest oxygen neighbors (Sabri et al. 2016). Fourier transform  
255 infrared spectra of  $\text{CoBi}_2\text{O}_4$  recorded within the range of 4000–400  $\text{cm}^{-1}$  are shown in  
256 Figure 5. It is evident in the IR spectrum that CBO had five intensive absorption peaks  
257 in the region of 400-900  $\text{cm}^{-1}$ , which could be related to the typical metal-oxygen (M–  
258 O) vibrations (Jasaitis et al. 2011). The presence of peaks between 570  $\text{cm}^{-1}$  and 669.9  
259  $\text{cm}^{-1}$  belonged to the vibration of the Bi–O bond and the vibration peak at 824.28  $\text{cm}^{-1}$   
260 can be assigned to Bi–O–Bi (Yang et al. 2018; Viruthagiri and Kannan 2019).  
261 Furthermore, the appearance of Peaks 446.13  $\text{cm}^{-1}$  and 532.31  $\text{cm}^{-1}$  can probably be  
262 related to the tetrahedral ( $\text{CoO}_4$ ) in the spinel (Sousa et al. 2019).

263 *Fig. 5 FTIR spectra of  $\text{CoBi}_2\text{O}_4$ .*

264 Figure 6 shows the Raman spectra of  $\text{CoBi}_2\text{O}_4$ . There are five Raman-activated  
265 bands; all these modes were observed at ambient conditions. The bands above 600  
266  $\text{cm}^{-1}$  were due to the motion of oxygen in the tetrahedral  $\text{AO}_4$  octahedral  $\text{BO}_6$  groups  
267 (Li et al. 2019a), suggesting a certain amount of Co and Bi disturbance in the  
268 tetrahedral and octahedral sites. The low-frequency modes observed at 54.13, 80.5  
269 and 123.73  $\text{cm}^{-1}$  can be related to the  $\text{Bi}^{3+}$  ion motion in the spinel layer and the mode  
270 at 521.03  $\text{cm}^{-1}$  can be attributed to the variation of bond distances between Bi atoms

271 and the spinel block apical O atoms (Zhang et al. 2018). The strongest band observed  
272 at  $264\text{ cm}^{-1}$  corresponded to O–Bi–O vibration (Zhang and Saxena 2013). The Raman  
273 modes of  $193.29$ ,  $476.05$ ,  $600$  and  $670\text{ cm}^{-1}$  were related to the vibration of the Co  
274 atoms (Diallo et al. 2015). Besides, a small Raman band was observed at  $151.35\text{ cm}^{-1}$ ;  
275 the origin of this band is still unknown.

276 *Fig. 6 Raman spectra of  $\text{CoBi}_2\text{O}_4$ .*

277 The morphology and structures of the prepared sample were visualized by  
278 Scanning Electron Micrograph (SEM) and transmission electron microscope (TEM)  
279 techniques were used. Figure 7 (a) shows a typical SEM image of the sample. It can  
280 be observed that the sample consisted of particles exhibiting cubic morphology. Due  
281 to the ultrafine nature of the sample, these particles displayed a slightly agglomerated  
282 morphology. The TEM images of  $\text{CoBi}_2\text{O}_4$  shown in figure 7 (b) demonstrate clear  
283 information regarding the size, shape and size distribution of nanoparticles. Based on  
284 the size distribution histogram in the inset figure, the catalyst was composed of particle  
285 size in the range of 22 nm. It was found that the size of the crystallite obtained from  
286 XRD analysis and the particle size obtained from TEM analysis were in the same size  
287 order. This picture also shows the existence of several aggregations within the range  
288 of nanometres.

289 The electron diffraction pattern of the nanoparticles are shown in figure 7 c, This  
290 pattern has a cubic shape and right angles ( $K/H = 1$ ,  $(\vec{H}, \vec{K}) = 90^\circ$ ) which is defined as  
291 a cubic face-centered CFC type of crystalline spinel (Andrews KW , Dyson DJ 1967)  
292 and that confirmed the XRD results.

293 *Fig. 7 SEM (a) TEM (b) Diffraction pattern (c) of nanoparticles  $\text{CoBi}_2\text{O}_4$ .*

294 The elementary study of the  $\text{CoBi}_2\text{O}_4$  nanoparticles was carried out by Energy  
295 Dispersive X-ray spectrometer (EDX). The peaks for Co, Bi and O elements were  
296 clearly observed in the EDX image, as shown in figure 8 (a). The atomic percentage of  
297 the elements in the sample are given in the inset Table of the EDX data. The atomic  
298 percentages of Co, Bi and O were estimated to be 14.02%, 26.25% and 59.73%,  
299 respectively. The quantification of Co, Bi and O confirmed that the atomic ratio of  
300 Co:Bi:O was 1.00:1.87:4.26, which agrees with the theoretical stoichiometric  
301 composition of  $\text{CoBi}_2\text{O}_4$ .

302 X-ray fluorescence measurements (XRF) spectra figure 8 (b) showed that Co  
303 and Bi were the most abundant elements. Regarding silver (Ag), it was used in the  
304 XRF analysis method. The inset Table of the XRF results shows that the weight  
305 percentage of CoO and Bi<sub>2</sub>O<sub>3</sub> was estimated to be (14.109%) for CoO and (85.89%)  
306 Bi<sub>2</sub>O<sub>3</sub>. The molar mass was then calculated for CoO and Bi<sub>2</sub>O<sub>3</sub> and found to be 74.93  
307 and 467.96 g/mol, respectively. This confirmed that the atomic ratio of Co:Bi:O was  
308 1.00:1.95:3.93, which agrees with the theoretical stoichiometric composition of  
309 CoBi<sub>2</sub>O<sub>4</sub> and also in line with the EDX analysis.

310 *Fig. 8 Energy dispersive X-ray (a) X-ray fluorescence (b) diffractogram of*  
311 *nanoparticles CoBi<sub>2</sub>O<sub>4</sub>.*

312 The elemental mappings in figure 9 were located in the same EDX region. The  
313 colored map of the SEM image (where Co, Bi and O are given in colors like Green,  
314 Red and Blue, respectively) revealed that Co, Bi, and O elements coexisted and were  
315 uniformly distributed.

316 *Fig. 9 EDX elemental mapping images of CoBi<sub>2</sub>O<sub>4</sub> a) All elements b) Cobalt c)*  
317 *Bismuth d) Oxygen.*

318 Optical properties of CoBi<sub>2</sub>O<sub>4</sub> nanostructure were measured using the UV–Vis  
319 diffuse reflectance spectrum. As shown in figure 10, the bandgap was estimated as  
320 2.5 eV which is lower than that of TiO<sub>2</sub> and ZnO (3.2 eV) (Serpone 2006; Miki-yoshida  
321 2016). This indicates that CBO has an excellent absorption level in the wavelength  
322 range from 300 to 800 nm that contains both UV and visible light, which appears more  
323 efficient than ZnO and TiO<sub>2</sub>, leading to an increase in the formation of electron-hole  
324 pairs on the photocatalyst's surface in visible light irradiation.

325 *Fig. 10 UV–Vis optical absorption edges.*

### 326 3.2 Artificial neural network modeling of the elimination of Cefixime

327 For the modeling, irradiation time, pH, initial CFX concentration and CBO catalyst  
328 dose were selected as the input variables and the related degradation rate of CFX was  
329 the output variable. To feed the structure of the ANN, a total of 40 experimental sets  
330 were used. The data sets have been divided into 70% training, 15% validation and  
331 15% test, as shown in Table 2.

332 *Table 2 Data sets of experimental results and ANN's predicted results.*

333 The essential part of the neural network architecture is the choice of the number  
334 of hidden neurons. The model's best performance comes when the mean square error  
335 (MSE) determined using equation (2), is the smallest.

336 *Fig. 11 Impact of the number of hidden neurons on the MSE of the neural network.*

337 Figure 11 shows that the Levenberg-Marquardt with a training function 'trainlim'  
338 and 13 hidden-layer neurons produced the highest correlation coefficient  $R^2 = 0.996$   
339 and the smallest MSE value  $1.81 \times 10^{-4}$ . The relation of experimental data to ANN  
340 model predictions can be derived from the contrast between the experimental data and  
341 the predictions of the ANN model (Fig.12). The training data were given as the model's  
342 input values, and the simulation output was compared with the relevant experimental  
343 data. The adaptation of the model results to experimental data for the training data set  
344 was very successful. The main part of model validation is the testing of network  
345 performance for the testing data set access, the correlation coefficient was likewise  
346 very high in this case  $R_{\text{test}}^2 = 0.977$ .

347 *Fig. 12 The relation of experimental data to the ANN model's predictions for each*  
348 *type of data.*

### 349 3.2.1 Effect of pH

350 The pharmaceuticals polluted water is discharged in the environment at variable  
351 pH values; consequently, it is necessary to investigate the role of pH on the  
352 photocatalytic degradation. For this purpose, photodegradation experiments have  
353 been carried out in 100 ml of 10 mg/L CFX solution at a fixed CBO amount of 0.1 g  
354 and 360 min irradiation. Three different initial pH was selected and kept constant by  
355 adding HCl or NaOH. The degradation rate of CFX increased with the increase of the  
356 pH value of the solution from 4 to 6 and then decreased from 6 to 8, as observed in  
357 figure 13 (a). Based on these results, it can be deduced that the photodegradation of  
358 CFX was optimal at pH = 6. It is difficult to grasp pH impact on the performance of the  
359 photocatalytic degradation process because of its multiple roles, such as the neutral  
360 electrical charge of the CFX molecules, as well as the protonation and the  
361 electropositive surface of CBO. This may also be related to the reaction between  
362 organic compounds and dissolved oxygen (Abbasi and Hasanpour 2017). The  
363 improvement of the photocatalytic activity of the catalyst at pH = 6 can probably be  
364 related to the charge accumulation on the external surface (Bai et al. 2017). So, the

365 pH change may therefore affect the dispersion of the catalyst in the suspension.  
366 Moreover, figure 13 (b) shows that the values predicted by the ANN model were well  
367 in line with the experimental data.

### 368 3.2.2 Effect of the catalyst dose

369 The effect of CBO catalyst dose on the photodegradation activity of CFX was  
370 examined. A set experiment was conducted by using a catalyst dose ranging from 0.05  
371 to 0.15 g in 100 mL of solution for 15 mg/L of CFX at pH = 6 and 360 min irradiation.  
372 Figure 13 (c) illustrates the effect of the catalyst dose on the CFX photodegradation  
373 removal, showing that the degradation of CFX increased from 66% to 72% for an  
374 increase of the catalyst dose from 0.05 to 0.08 g because of the limited active sites  
375 available on the CBO catalyst surface. However, the degradation efficiency of CFX  
376 decreased beyond this amount of catalyst, namely from 0.08 to 0.15 g. This may be  
377 attributed to the fact that the accumulation of free catalysts leads to an increase in the  
378 opacity of the solution and a decrease in light penetration. This is due to a scattering  
379 effect for an expansion of the dose of catalyst (Zhou et al. 2018). Therefore, the optimal  
380 dosage of the catalyst for CFX photodegradation was selected to be 0.08 g. Based on  
381 the obtained results shown in figure 13 (d), the results predicted by the ANN and the  
382 experimental values were well agreed.

### 383 3.2.3 Effect of the initial CFX concentration

384 For the purpose, the photodegradation studies were performed by varying initial  
385 concentrations of CFX from 5 to 15 mg/L in 100 ml of the solution with 0.1 g of the CBO  
386 catalyst at pH 6 after 360 min of irradiation time under visible light. Figure 13 (e) shows  
387 that by raising the CFX concentration, the degradation yield decreased from 82 to 55%.  
388 This behavior can be related to the diminishing number of available sites on the catalyst  
389 CBO surface. Therefore, a high number of CFX molecules would have an inhibitory  
390 effect on the photodegradation efficiency due to the lack of any direct contact between  
391 the CBO catalyst surface and CFX. Besides, many photons could be absorbed by the  
392 CFX molecules and hence did not reach the catalyst surface. The comparison between  
393 ANN predicted values and the experimental data shown in figure 13 (f) revealed a good  
394 agreement between them.

395 Fig. 13 (a) effect pH (c) effect of catalyst dose (e) effect of initial CFX concentration  
396 (b,d,f) Comparison of the experimental results with the predicted ANN values for  
397 various operating parameters.

### 398 3.2.4 The relative significance

399 An evaluation process based on the network weight matrix and the Garson's  
400 equation (Garson 1991) was applied to calculate the relative significance of the input  
401 variables on the network's output. The relative significance of input variables  
402 influencing the CFX photodegradation values has been calculated by equation 6  
403 (Ibrahim 2013).

$$RI_X = \sum_{x=1}^n \frac{|w_{xy}w_{yz}|}{\sum_{y=1}^m |w_{xy}w_{yz}|} \quad (6)$$

404 where  $RI_X$  is the relative significance,  $n$  and  $m$  are respectively the input numbers and  
405 hidden neurons.  $w_{xy}$  are the connection weights,  $\sum_{y=1}^m |w_{xy}w_{yz}|$  is the sum of the  
406 product of the final weights of the connections from input neurons to hidden neurons  
407 along with the links from hidden neurons to output neurons (Ibrahim 2013).

408 *Table 3 ANN model's weight and bias matrix.*

409 The ANN model's weight matrix is given in Table 3, while the relative significance of  
410 the input variables derived from equation (4) is displayed in figure 14. As can be seen,  
411 the initial CFX concentration showed the most significant impact on the performance  
412 of CFX photodegradation (28%) compared with the other operating factors, namely  
413 CBO dosage (27%), irradiation time (24%) and pH (21%).

414 *Fig. 14 The relative significance of the inputs on CFX degradation.*

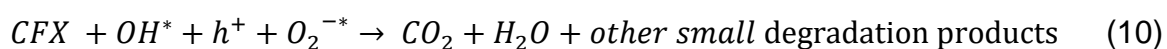
### 415 3.3 Effect of scavenging agents and the photocatalytic mechanism

416 Generally, the photodegradation of organic compounds by a catalyst semi-  
417 conductor can be described by different reaction pathways regulated by different active  
418 species such as  $\text{OH}^\bullet$  hydroxyl radical, superoxide  $\text{O}_2^\bullet$ , and photogenerated electrons  
419 and holes  $e^-/h^+$  pairs which called reactive oxidant species (ROS) (Zuo et al. 2017).  
420 To investigate the dominant ROS on the photodegradation of Cefixime over the CBO  
421 catalyst and for an understanding of the photocatalytic mechanism, several active  
422 species trapping tests were run in the presence of different concentrations of some

423 scavengers. Each of the scavenging species was chosen for a specific type of  
 424 photocatalytic radicals. p-Benzoquinone BQ was used as superoxide  $O_2^*$  radical  
 425 quencher ( a scavenger for superoxide anion radical) (Nithya and Ayyappan 2020),  
 426 Potassium dichromate  $K_2Cr_2O_7$  was used as a scavenger for electron ( $e^-$ ) (Gupta et  
 427 al. 2020), Disodium ethylenediaminetetraacetic acid ( $Na_2$ -EDTA) was used as a  
 428 scavenger for the hole ( $h^+$ ) and as photoinduced  $h^+$  acceptor (Tho et al. 2020) and  
 429 isopropanol (IPA) alcohol was employed as an  $OH^*$  scavenger (hydroxyl  $OH^*$  radical  
 430 quencher) (Ghattavi and Nezamzadeh-Ejhih 2020). The tests were performed with  
 431 an initial Cefixime concentration of 5 mg/L, at pH 6, and using CBO with a solution ratio  
 432 of 0.8 g/L. The impact of these scavenging agents (quenchers) on the  
 433 photodegradation efficiency of CBO nanocomposite was shown in Fig 15.

434 *Fig. 15 Effect of different scavengers on photocatalytic degradation of CFX over CBO*  
 435 *photocatalyst.*

436 The obtained results are summarized in the next order of the photodegradation  
 437 efficiency in the presence of different scavengers: Sample without the scavengers  
 438 (Free) (79 %) >  $K_2Cr_2O_7$  (64%) > p-Benzoquinone (59%) >  $Na_2$ -EDTA (40%) >  
 439 Isopropanol (25%). As shown, the most decrease in the degradation efficiency was  
 440 observed by Isopropanol which confirmed that the generated  $OH^*$  has a dominant role  
 441 in the degradation of CFX.  $OH^*$  radicals are strong, active and unselected oxidizing  
 442 species for organic substrates in terms of oxidative degradation (Kumar et al. 2020).  
 443 Then it comes  $Na_2$ -EDTA, this indicates that both  $OH^*$  and  $h^+$  are the major active  
 444 species. However, in the presence of p-Benzoquinone, only a small effect has been  
 445 observed on the CFX photodegradation. This indicates that  $O_2^*$  was a minor active  
 446 species. The effect of  $K_2Cr_2O_7$  was so small that it neglected the electron  $e^-$  role in the  
 447 CFX degradation. According to these results, the following pathways (Fig. 16 and  
 448 equations 7,8,9 and 10) were suggested for the photodegradation of CFX onto CBO.



449 *Fig. 16 Proposed mechanism for CFX degradation in the presence of  $CoBi_2O_4$*   
 450 *nanoparticles.*



### 451 3.4 Comparison of Cefixime photodegradation by different processes

452 In order to enhance the photocatalytic performance of CFX by synthesized CBO  
453 nanoparticles and also to eliminate the photolysis effect, a set of experiments have  
454 been tested in the same condition as illustrated in fig.17. The experiment was  
455 conducted in the presence of 0.1 g catalyst at pH 6, room temperature and an initial  
456 CFX concentration of 10 mg/L. In the absence of the catalyst, a very small degradation  
457 rate of CFX by photolysis can be observed, lower than 5%. On the other hand, in the  
458 presence of the CBO photocatalyst, the degradation rate of CFX reached 60 % within  
459 3 h. The hetero-systems can increase the rate of photo-activity by extending the  
460 spectral photo response of wide band semiconductors toward the visible light region,  
461 as already demonstrated in recent works (Belaissa et al. 2016; Boumaza et al. 2016;  
462 Rekhila et al. 2017; Boutra et al. 2019). For that, the new hetero-system  $\text{CoBi}_2\text{O}_4/\text{ZnO}$   
463 has been tested. Different weight ratios of the two catalysts CBO and ZnO were tested  
464 to examine the impact on the CFX photodegradation. As can be seen in fig.17, the high  
465 photodegradation efficiency was noticed at ratio of 50%/50% weight percentage of the  
466 hetero-system  $\text{CoBi}_2\text{O}_4/\text{ZnO}$ , leading to an 80% degradation efficiency within only 3 h.

467 *Fig. 17 Time-course of the CFX degradation by different processes.*

### 468 4. Conclusion

469 In summary, in the present work,  $\text{CoBi}_2\text{O}_4$  nanoparticles were successfully  
470 synthesized by the sol-gel method and then characterized by both spectroscopic and  
471 morphological tools. The catalysts prepared were tested for CFX antibiotic  
472 degradation. The photocatalytic degradation of CFX was modeled successfully using  
473 an artificial neural network (ANN). A feed-forward neural network with backpropagation  
474 method and a Levenberg-Marquardt method was used. The degradation of CFX in  
475 different operating conditions was predicted with 13 hidden neurons. The results  
476 showed that the  $\text{CoBi}_2\text{O}_4$  nanoparticles led to an 86 % CFX photodegradation yield in  
477 the following optimal condition, pH = 6, 5 mg/L CFX, 0.8 g/L catalyst dose and 360 min  
478 of irradiation. It was shown that all the parameters of the study (irradiation time, pH,  
479 initial concentration of CFX and catalyst dose) have a significant effect on the CFX  
480 photodegradation.

481 However, the main effect was the CFX's initial concentration. Moreover, the effects  
482 of some scavenging agents were studied and the results confirmed the dominant role

483 of hydroxyl radical OH• in the CFX degradation process. Finally, the new CoBi<sub>2</sub>O<sub>4</sub>/ZnO  
484 hetero-system was discussed and demonstrated a rapid degradation efficiency of 80  
485 % in just 3 hours. Owing to these promising preliminary results, it will be further  
486 considered in future works.

#### 487 **Acknowledgment**

488 The authors gratefully acknowledge the financial support from the Thematic  
489 Research Agency for Science and Technology (ATRST) through the national research  
490 program (PM, PRFU Project N°A16N01UN160420190002) and the Directorate-  
491 General for Scientific Research and Technological Development (DGRSDT) of Algeria.

#### 493 **Declaration**

494

#### 495 **Ethics approval and consent to participate**

496 Not applicable

497

#### 498 **Consent for publication**

499 Not applicable

500

#### 501 **Competing interest**

502 The authors declare that they have no conflict of interest.

503

#### 504 **Authors contributions**

505 *Oussama Baaloudj and Mohamed Kebir*: investigation, formal analysis, visualization,  
506 writing original draft.

507 *Noureddine Nasrallah and Aymen Amin Assadi*: conceptualization, funding acquisition,  
508 methodology, resources, project administration, supervision, writing-review and  
509 editing.

510 *Phuong Nguyen-Tri*: writing-review and editing, methodology, conceptualization.

511 *Bouzid Guedioura*: formal analysis

512 *Abdeltif Amrane and Sonil Nanda*: investigation, visualization.

513

#### 514 **Availability of data and materials:**

515 The datasets used and/or analysed during the current study are available from the  
516 corresponding author on reasonable request.

517

## 518 **References**

519

520 Abbasi S, Hasanpour M (2017) The effect of pH on the photocatalytic degradation of  
521 methyl orange using decorated ZnO nanoparticles with SnO<sub>2</sub> nanoparticles. *J*  
522 *Mater Sci Mater Electron* 28:1307–1314. [https://doi.org/10.1007/s10854-016-](https://doi.org/10.1007/s10854-016-5660-5)  
523 [5660-5](https://doi.org/10.1007/s10854-016-5660-5)

524 Aboudalle A, Fourcade F, Assadi AA, et al (2018) Reactive oxygen and iron species  
525 monitoring to investigate the electro-Fenton performances. Impact of the  
526 electrochemical process on the biodegradability of metronidazole and its by-  
527 products. *Chemosphere* 199:486–494.  
528 <https://doi.org/10.1016/j.chemosphere.2018.02.075>

529 Andrews KW , Dyson DJ KS (1967) Interpretation of electron diffraction patterns

530 Ayodele BV, Alsaffar MA, Mustapa SI, Vo DVN (2020) Backpropagation neural  
531 networks modelling of photocatalytic degradation of organic pollutants using  
532 TiO<sub>2</sub>-based photocatalysts. *J Chem Technol Biotechnol*.  
533 <https://doi.org/10.1002/jctb.6407>

534 Ayoubi-Feiz B, Sheydaei M, Karimi M (2019) Visible light photoelectrocatalysis for  
535 wastewater treatment using bifacial N-TiO<sub>2</sub>/Graphene/H<sub>2</sub>O<sub>2</sub>/Titanium  
536 nanocomposite: Artificial neural network modeling and evaluation of ozone  
537 addition. *Process Saf Environ Prot* 127:56–65.  
538 <https://doi.org/10.1016/j.psep.2019.04.026>

539 Bai Y, Huang H, Wang C, et al (2017) Engineering the surface charge states of  
540 nanostructures for enhanced catalytic performance. *Mater Chem Front* 1:1951–  
541 1964. <https://doi.org/10.1039/c7qm00020k>

542 Diallo A, Beye AC, Doyle TB, et al (2015) Green synthesis of Co<sub>3</sub>O<sub>4</sub> nanoparticles  
543 via *Aspalathus linearis*: Physical properties. *Green Chem Lett Rev* 8:30–36.  
544 <https://doi.org/10.1080/17518253.2015.1082646>

545 Elder FCT, Feil EJ, Snape JN, et al (2020) The role of stereochemistry of antibiotic

546 agents in the development of antibiotic resistance in the environment. *Environ Int*  
547 139:105681. <https://doi.org/10.1016/j.envint.2020.105681>

548 Garg A, Kaur G, Sangal VK, et al (2020) Optimization methodology based on neural  
549 networks and box - behnken design applied to photocatalysis of acid red. 0–2.  
550 <https://doi.org/10.4491/eer.2019.246>

551 Garson GD (1991) Interpreting neural-network connection weights. *AI Expert* 6:46–51

552 Ghattavi S, Nezamzadeh-Ejhieh A (2020) A visible light driven AgBr/g-C3N4  
553 photocatalyst composite in methyl orange photodegradation: Focus on  
554 photoluminescence, mole ratio, synthesis method of g-C3N4 and scavengers.  
555 *Compos Part B Eng* 183:107712.  
556 <https://doi.org/10.1016/j.compositesb.2019.107712>

557 Giannopoulou I, Saï s F, Thomopoulos R (2015) Handbook-of-pharmaceutical-  
558 excipients-6th-edition. *Rev des Nouv Technol l'Information E.*28:257–262

559 Gupta NK, Ghaffari Y, Kim S, et al (2020) Photocatalytic Degradation of Organic  
560 Pollutants over MFe2O4 (M = Co, Ni, Cu, Zn) Nanoparticles at Neutral pH. *Sci*  
561 *Rep* 10:1–11. <https://doi.org/10.1038/s41598-020-61930-2>

562 Hassani A, Khataee A, Karaca S (2015) Photocatalytic degradation of ciprofloxacin  
563 by synthesized TiO2 nanoparticles on montmorillonite: Effect of operation  
564 parameters and artificial neural network modeling. *J Mol Catal A Chem* 409:149–  
565 161. <https://doi.org/10.1016/j.molcata.2015.08.020>

566 Hazrati H, Moghaddam AH, Rostamizadeh M (2017) The influence of hydraulic  
567 retention time on cake layer specifications in the membrane bioreactor:  
568 Experimental and artificial neural network modeling. *J Environ Chem Eng*  
569 5:3005–3013. <https://doi.org/10.1016/j.jece.2017.05.050>

570 Homem V, Santos L (2011) Degradation and removal methods of antibiotics from  
571 aqueous matrices - A review. *J Environ Manage* 92:2304–2347.  
572 <https://doi.org/10.1016/j.jenvman.2011.05.023>

573 Ibáñez M, Borova V, Boix C, et al (2017) UHPLC-QTOF MS screening of  
574 pharmaceuticals and their metabolites in treated wastewater samples from  
575 Athens. *J Hazard Mater* 323:26–35.

576 <https://doi.org/10.1016/j.jhazmat.2016.03.078>

577 Ibrahim OM (2013) A comparison of methods for assessing the relative importance of  
578 input variables in artificial neural networks. *J Appl Sci Res* 9:5692–5700.  
579 <https://doi.org/10.1067/mmt.2002.123333>

580 Jagadeesh C, Sailaja BB V (2019) Photocatalytic Degradation of Rhodamine B Dye  
581 using CoBi<sub>2</sub>O<sub>4</sub> Nanocatalyst and Effect of Various Operational Parameters.  
582 *CIKITUSI J* 6:97–107

583 Jasaitis D, Beganskiene A, Senvaitiene J, et al (2011) Sol-gel synthesis and  
584 characterization of cobalt chromium spinel CoCr<sub>2</sub>O<sub>4</sub>. *Chemija* 22:125–130.  
585 <https://doi.org/10.1039/c3ce41663a>

586 Kaczala F, E. Blum S (2015) The Occurrence of Veterinary Pharmaceuticals in the  
587 Environment: A Review. *Curr Anal Chem* 12:169–182.  
588 <https://doi.org/10.2174/1573411012666151009193108>

589 Kamagate M, Amin Assadi A, Kone T, et al (2018) Activation of persulfate by  
590 irradiated laterite for removal of fluoroquinolones in multi-component systems. *J*  
591 *Hazard Mater* 346:159–166. <https://doi.org/10.1016/j.jhazmat.2017.12.011>

592 Kaur R, Kaur B (2014) Artificial Neural Network Learning Enhancement using  
593 Bacterial Foraging Optimization Algorithm. *Int J Comput Appl* 102:27–33.  
594 <https://doi.org/10.5120/17852-8812>

595 Kumar R, Barakat MA, Al-Mur BA, et al (2020) Photocatalytic degradation of cefoxitin  
596 sodium antibiotic using novel BN/CdAl<sub>2</sub>O<sub>4</sub> composite. *J Clean Prod* 246:119076.  
597 <https://doi.org/10.1016/j.jclepro.2019.119076>

598 Li K, Luo Y, Liu B, et al (2019a) High-performance NO<sub>2</sub>-gas sensing of ultrasmall  
599 ZnFe<sub>2</sub>O<sub>4</sub> nanoparticles based on surface charge transfer. *J Mater Chem A*  
600 7:5539–5551. <https://doi.org/10.1039/c8ta12168k>

601 Li Q, Jia R, Shao J, He Y (2019b) Photocatalytic degradation of amoxicillin via TiO<sub>2</sub>  
602 nanoparticle coupling with a novel submerged porous ceramic membrane  
603 reactor. *J Clean Prod* 209:755–761. <https://doi.org/10.1016/j.jclepro.2018.10.183>

604 Littmann J, Buyx A, Cars O (2015) Antibiotic resistance: An ethical challenge. *Int J*  
605 *Antimicrob Agents* 46:359–361. <https://doi.org/10.1016/j.ijantimicag.2015.06.010>

- 606 Liu M, Ni H, Yang L, et al (2019) Pretreatment of swine manure containing  $\beta$ -lactam  
607 antibiotics with whole-cell biocatalyst to improve biogas production. *J Clean Prod*  
608 240:118070. <https://doi.org/10.1016/j.jclepro.2019.118070>
- 609 Lou W, Kane A, Wolbert D, et al (2017) Study of a photocatalytic process for removal  
610 of antibiotics from wastewater in a falling film photoreactor: Scavenger study and  
611 process intensification feasibility. *Chem Eng Process Process Intensif* 122:213–  
612 221. <https://doi.org/10.1016/j.cep.2017.10.010>
- 613 Medarević DP, Kleinebudde P, Djuriš J, et al (2016) Combined application of mixture  
614 experimental design and artificial neural networks in the solid dispersion  
615 development. *Drug Dev Ind Pharm* 42:389–402.  
616 <https://doi.org/10.3109/03639045.2015.1054831>
- 617 Miki-yoshida M (2016) Optical Band Gap Estimation of ZnO Nanorods a  $E = B \wedge E -$   
618 Eg h. 19:33–38. <https://doi.org/10.1590/1980-5373-mr-2015-0612>
- 619 Mirzaei R, Yunesian M, Nasser S, et al (2018) Occurrence and fate of most  
620 prescribed antibiotics in different water environments of Tehran, Iran. *Sci Total*  
621 *Environ* 619–620:446–459. <https://doi.org/10.1016/j.scitotenv.2017.07.272>
- 622 Mohammadzadeh Kakhki R, Mohammadpoor M, Faridi R, Bahadori M (2020) The  
623 development of an artificial neural network-genetic algorithm model (ANN-GA)  
624 for the adsorption and photocatalysis of methylene blue on a novel sulfur-  
625 nitrogen co-doped Fe<sub>2</sub>O<sub>3</sub> nanostructure surface. *RSC Adv* 10:5951–5960.  
626 <https://doi.org/10.1039/c9ra10349j>
- 627 Mostafaloo R, Mahmoudian MH, Asadi-ghalhari M (2019) BiFeO<sub>3</sub> / Magnetic  
628 nanocomposites for the photocatalytic degradation of ce fi xime from aqueous  
629 solutions under visible light. *J Photochem Photobiol A Chem* 382:111926.  
630 <https://doi.org/10.1016/j.jphotochem.2019.111926>
- 631 Nguyen CH, Fu CC, Juang RS (2018) Degradation of methylene blue and methyl  
632 orange by palladium-doped TiO<sub>2</sub> photocatalysis for water reuse: Efficiency and  
633 degradation pathways. *J Clean Prod* 202:413–427.  
634 <https://doi.org/10.1016/j.jclepro.2018.08.110>
- 635 Nithya R, Ayyappan S (2020) Novel exfoliated graphitic-C<sub>3</sub>N<sub>4</sub> hybridised ZnBi<sub>2</sub>O<sub>4</sub>  
636 (g-C<sub>3</sub>N<sub>4</sub>/ZnBi<sub>2</sub>O<sub>4</sub>) nanorods for catalytic reduction of 4-Nitrophenol and its

637 antibacterial activity. *J Photochem Photobiol A Chem* 398:  
638 <https://doi.org/10.1016/j.jphotochem.2020.112591>

639 Raou D (2017) Synthesis and microstructural properties of ZnO nanoparticles  
640 prepared by precipitation method Synthesis and microstructural properties of  
641 ZnO nanoparticles prepared by precipitation method. *Renew Energy* 50:932–  
642 937. <https://doi.org/10.1016/j.renene.2012.08.076>

643 Sabri K, Rais A, Taibi K, et al (2016) Structural Rietveld refinement and vibrational  
644 study of  $MgCr_xFe_{2-x}O_4$  spinel ferrites. *Phys B Condens Matter* 501:38–44.  
645 <https://doi.org/10.1016/j.physb.2016.08.011>

646 Sample I (2018) Calls to rein in antibiotic use after study shows 65% increase  
647 worldwide. In: *Guard*. [https://www.theguardian.com/science/2018/mar/26/calls-](https://www.theguardian.com/science/2018/mar/26/calls-to-rein-in-antibiotic-use-after-study-shows-65-increase-worldwide)  
648 [to-rein-in-antibiotic-use-after-study-shows-65-increase-worldwide](https://www.theguardian.com/science/2018/mar/26/calls-to-rein-in-antibiotic-use-after-study-shows-65-increase-worldwide). Accessed 26  
649 Mar 2018

650 Sayadi MH, Sobhani S, Shekari H (2019) Photocatalytic degradation of azithromycin  
651 using GO@Fe<sub>3</sub>O<sub>4</sub>/ ZnO/ SnO<sub>2</sub> nanocomposites. *J Clean Prod* 232:127–136.  
652 <https://doi.org/10.1016/j.jclepro.2019.05.338>

653 Serpone N (2006) Is the band gap of pristine TiO<sub>2</sub> narrowed by anion- and cation-  
654 doping of titanium dioxide in second-generation photocatalysts? *J Phys Chem B*  
655 110:24287–24293. <https://doi.org/10.1021/jp065659r>

656 Sheydaei M, Shiadeh HRK, Ayoubi-Feiz B, Ezzati R (2018) Preparation of nano N-  
657 TiO<sub>2</sub>/graphene oxide/titan grid sheets for visible light assisted photocatalytic  
658 ozonation of cefixime. *Chem Eng J* 353:138–146.  
659 <https://doi.org/10.1016/j.cej.2018.07.089>

660 Shokoohi R, Leili M, Dargahi A, et al (2017) Common Antibiotics in Wastewater of  
661 Sina and Besat Hospitals, Hamadan, Iran. *Arch Hyg Sci* 6:152–159.  
662 <https://doi.org/10.29252/archhygsci.6.2.152>

663 Shooshtari NM, Ghazi MM (2017) An investigation of the photocatalytic activity of  
664 nano A-Fe<sub>2</sub>O<sub>3</sub>/ZnO on the photodegradation of cefixime trihydrate. *Chem Eng J*  
665 315:527–536. <https://doi.org/10.1016/j.cej.2017.01.058>

666 Sousa OM, Lima JS, Lima AF, Lalic M V. (2019) Theoretical study of structural,

667 electronic and magnetic properties of the spinel  $\text{Co}_3\text{O}_4$  under the pressure  
668 from 0 to 30 GPa. *J Magn Mater* 484:21–30.  
669 <https://doi.org/10.1016/j.jmmm.2019.03.122>

670 Tabatabai-Yazdi FS, Ebrahimian Pirbazari A, Esmaili Khalilsaraei F, et al (2019)  
671 Photocatalytic treatment of tetracycline antibiotic wastewater by silver/ $\text{TiO}_2$   
672 nanosheets/reduced graphene oxide and artificial neural network modeling.  
673 *Water Environ Res*. <https://doi.org/10.1002/wer.1258>

674 Tho NTM, Khanh DNN, Thang NQ, et al (2020) Novel reduced graphene  
675 oxide/ $\text{ZnBi}_2\text{O}_4$  hybrid photocatalyst for visible light degradation of 2,4-  
676 dichlorophenoxyacetic acid. *Environ Sci Pollut Res* 27:11127–11137.  
677 <https://doi.org/10.1007/s11356-020-07752-1>

678 Viruthagiri G, Kannan P (2019) Visible light mediated photocatalytic activity of cobalt  
679 doped  $\text{Bi}_2\text{O}_3$  nanoparticles. *J Mater Res Technol* 8:127–133.  
680 <https://doi.org/10.1016/j.jmrt.2017.06.011>

681 World Health Organisation (2011) Tackling antibiotic resistance from a food safety  
682 perspective in Europe. *World Heal Organ* 1–88

683 Xiong W, Zeng G, Yang Z, et al (2018) Adsorption of tetracycline antibiotics from  
684 aqueous solutions on nanocomposite multi-walled carbon nanotube  
685 functionalized MIL-53(Fe) as new adsorbent. *Sci Total Environ* 627:235–244.  
686 <https://doi.org/10.1016/j.scitotenv.2018.01.249>

687 Yang J, Xie T, Liu C, Xu L (2018) Facile fabrication of dumbbell-like  $\beta\text{-Bi}_2\text{O}_3$ /  
688 graphene nanocomposites and their highly efficient photocatalytic activity.  
689 *Materials (Basel)* 11:.. <https://doi.org/10.3390/ma11081359>

690 Zhang FX, Saxena SK (2013) Raman studies of  $\text{Bi}_2\text{CuO}_4$  at high pressures.  
691 141926:2–5. <https://doi.org/10.1063/1.2189450>

692 Zhang H, Ke H, Ying P, et al (2018) Crystallisation process of  $\text{Bi}_5\text{Ti}_3\text{FeO}_{15}$   
693 multiferroic nanoparticles synthesised by a sol–gel method. *J Sol-Gel Sci*  
694 *Technol* 85:132–139. <https://doi.org/10.1007/s10971-017-4530-9>

695 Zhang X, Zhang Y, Ngo HH, et al (2020) Characterization and sulfonamide antibiotics  
696 adsorption capacity of spent coffee grounds based biochar and hydrochar. *Sci*



697 Total Environ 716:.. <https://doi.org/10.1016/j.scitotenv.2020.137015>

698 Zhou C, Wang Q, Zhou C (2020) Photocatalytic degradation of antibiotics by  
699 molecular assembly porous carbon nitride: Activity studies and artificial neural  
700 networks modeling. Chem Phys Lett 750:137479.  
701 <https://doi.org/10.1016/j.cplett.2020.137479>

702 Zhou F, Yan C, Liang T, et al (2018) Photocatalytic degradation of Orange G using  
703 sepiolite-TiO<sub>2</sub> nanocomposites: Optimization of physicochemical parameters  
704 and kinetics studies. Chem Eng Sci 183:231–239.  
705 <https://doi.org/10.1016/j.ces.2018.03.016>

706 Zhu H, Chen T, Liu J, Li D (2018) Adsorption of tetracycline antibiotics from an  
707 aqueous solution onto graphene oxide/calcium alginate composite fibers. RSC  
708 Adv 8:2616–2621. <https://doi.org/10.1039/c7ra11964j>

709 Zulfiqar M, Samsudin MFR, Sufian S (2019) Modelling and optimization of  
710 photocatalytic degradation of phenol via TiO<sub>2</sub> nanoparticles: An insight into  
711 response surface methodology and artificial neural network. J Photochem  
712 Photobiol A Chem 384:112039.  
713 <https://doi.org/10.1016/j.jphotochem.2019.112039>

714 Zuo S, Chen Y, Liu W, et al (2017) A facile and novel construction of  
715 attapulgite/Cu<sub>2</sub>O/Cu/g-C<sub>3</sub>N<sub>4</sub> with enhanced photocatalytic activity for antibiotic  
716 degradation. Ceram Int 43:3324–3329.  
717 <https://doi.org/10.1016/j.ceramint.2016.11.173>

718

**Table 1** ANN model parameters.

Parameters	Value
Input Neurons	pH, time, dose CBO, concentration of CFX
Output Neurons	Degradation of CFX
Number of Hidden Layer	(2-20) selection based on minimum MSE
Training function	Levenberg-Marquardt
Number experiment points	40 points
Performance function	MSE
Data division	70%-15%-15%

**Table 2** Data sets of experimental results and ANN's predicted results.

Run	Time (min)	pH	CFC (ppm)	photocatalyst (g/l)	photodegradation (%)	
					Actual	Predicted
1	30	6	10	1	0.1281	0.1303
2	360	6	15	1	0.5471	0.5501
3	120	6	10	1	0.4812	0.4831
4	30	6	15	0.75	0.1065	0.1087
5	240	6	10	1	0.6813	0.6816
6	240	6	12.5	1	0.5814	0.5742
7	360	6	10	1	0.7031	0.699
8	60	6	15	1.5	0.1238	0.1229
9	240	4	10	1	0.5378	0.5382
10	300	8	10	1	0.6216	0.6205
11	360	8	10	1	0.6445	0.6484
12	300	6	15	1.5	0.4857	0.4864
13	180	4	10	1	0.4538	0.454
14	300	6	15	0.75	0.5017	0.5027
15	60	4	10	1	0.1387	0.1403
16	120	6	15	1.5	0.2286	0.2286
17	360	4	10	1	0.5588	0.5753
18	120	6	15	0.5	0.3464	0.3529
19	360	6	15	1.5	0.5238	0.5521
20	60	6	12.5	1	0.2093	0.2002
21	180	6	15	0.5	0.3954	0.4005
22	120	6	15	1	0.3134	0.3162
23	120	6	15	0.75	0.3471	0.3442
24	360	6	15	0.5	0.4444	0.4585
25	300	6	15	0.5	0.45	0.4448
26	360	6	15	0.75	0.502	0.504
27	300	6	15	1	0.538	0.5336
28	60	8	10	1	0.1972	0.1965
29	60	6	15	1	0.183	0.1828
30	180	8	10	1	0.4954	0.4832
31	60	6	5	1	0.4468	0.4464
32	300	4	10	1	0.5588	0.5592
33	240	6	15	1	0.4928	0.503
34	30	6	5	1	0.1844	0.282
35	240	6	5	1	0.8227	0.8208
36	300	6	10	1	0.6969	0.7056
37	360	6	5	1	0.8227	0.824
38	180	6	10	1	0.6	0.6174
39	60	6	15	0.5	0.2647	0.2456
40	60	6	10	1	0.2469	0.2497

**Table 3** ANN model's weight and bias matrix.

Neurons of hidden layer	Weights and biases between input and hidden layers					Weights and biases between hidden and output layers	
	Input variables					Output Degradation Rate %	Bias
	Radiation time	pH	Initial concentration of CFX	Catalyst dosage	Bias		
<b>1</b>	-0.209	-0.155	-2.371	-1.364	2.586	0.258	
<b>2</b>	-0.524	-1.142	-1.34	-1.544	2.318	-0.514	
<b>3</b>	-1.669	1.438	1.281	-1.376	1.922	0.081	
<b>4</b>	1.204	1.295	-1.615	0.709	-0.558	0.515	
<b>5</b>	-1.58	0.183	1.387	-1.792	1.284	0.217	
<b>6</b>	-1.005	-1.551	-1.256	1.273	0.359	0.117	
<b>7</b>	1.407	-1.721	-0.843	-0.515	-0.531	-0.157	-0.29
<b>8</b>	-0.0028	-1.191	-1.811	-0.459	-0.645	0.3	
<b>9</b>	-1.107	-1.116	-0.201	-1.503	-0.872	-0.277	
<b>10</b>	-0.5608	1.804	-0.763	1.813	-1.227	-0.721	
<b>11</b>	2.053	0.782	-0.303	-0.83	1.619	0.71	
<b>12</b>	1.637	-0.136	-1.36	-1.151	2.809	-0.614	
<b>13</b>	1.435	0.1417	-1.93	-1.541	2.271	0.231	

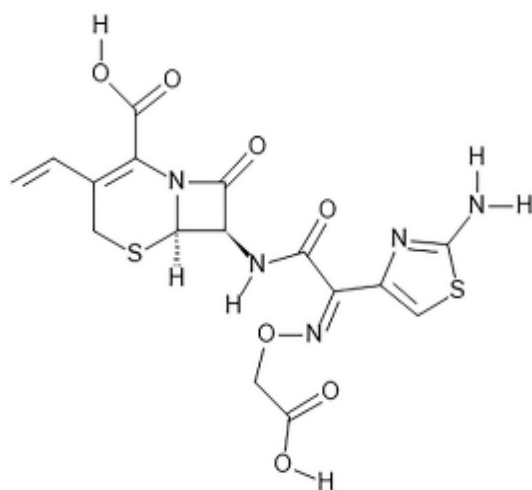


Fig. 1

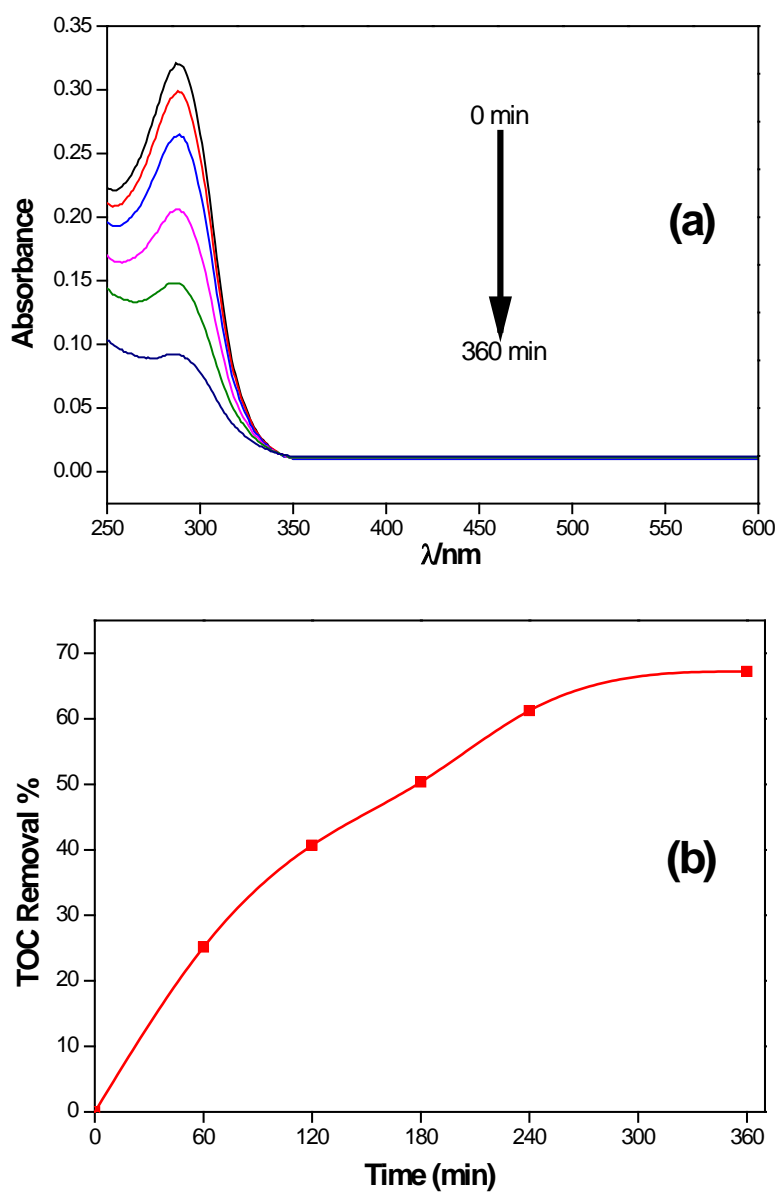


Fig. 2

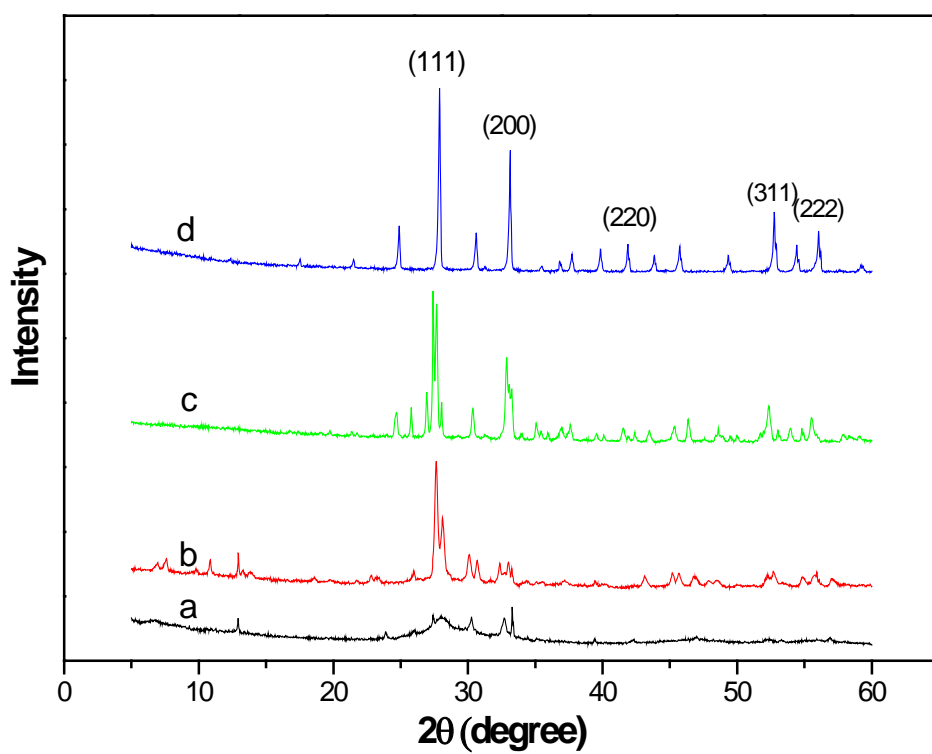


Fig. 3

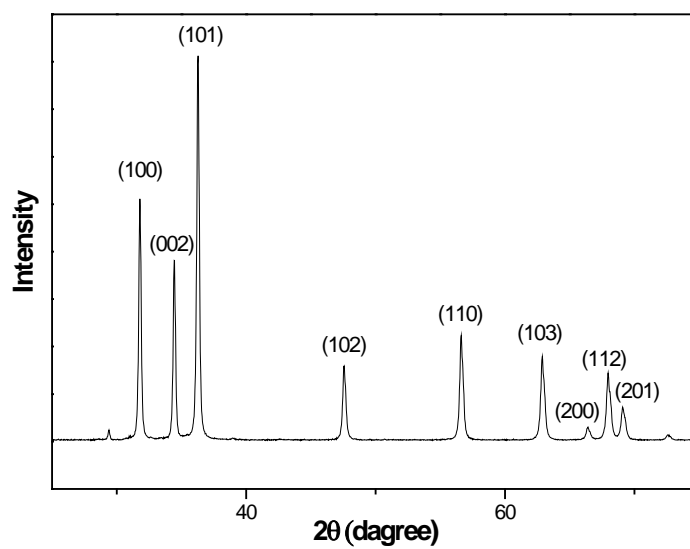


Fig. 4

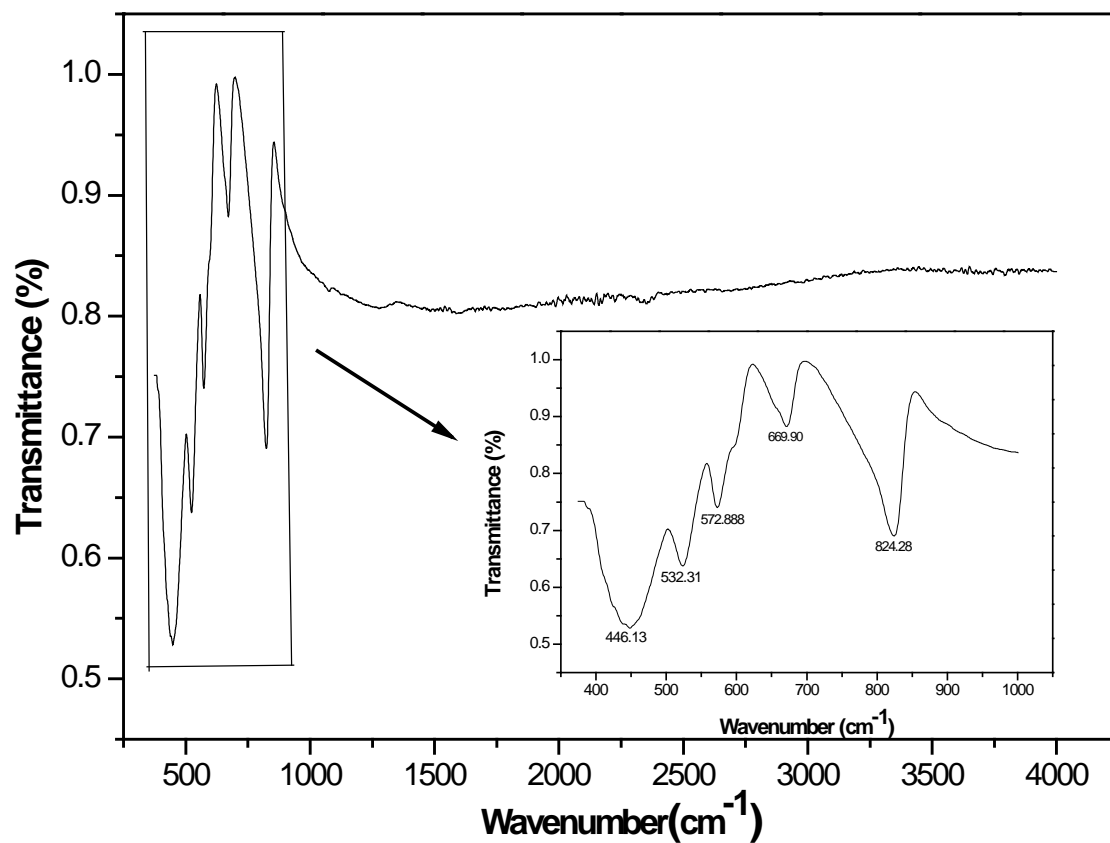


Fig. 5

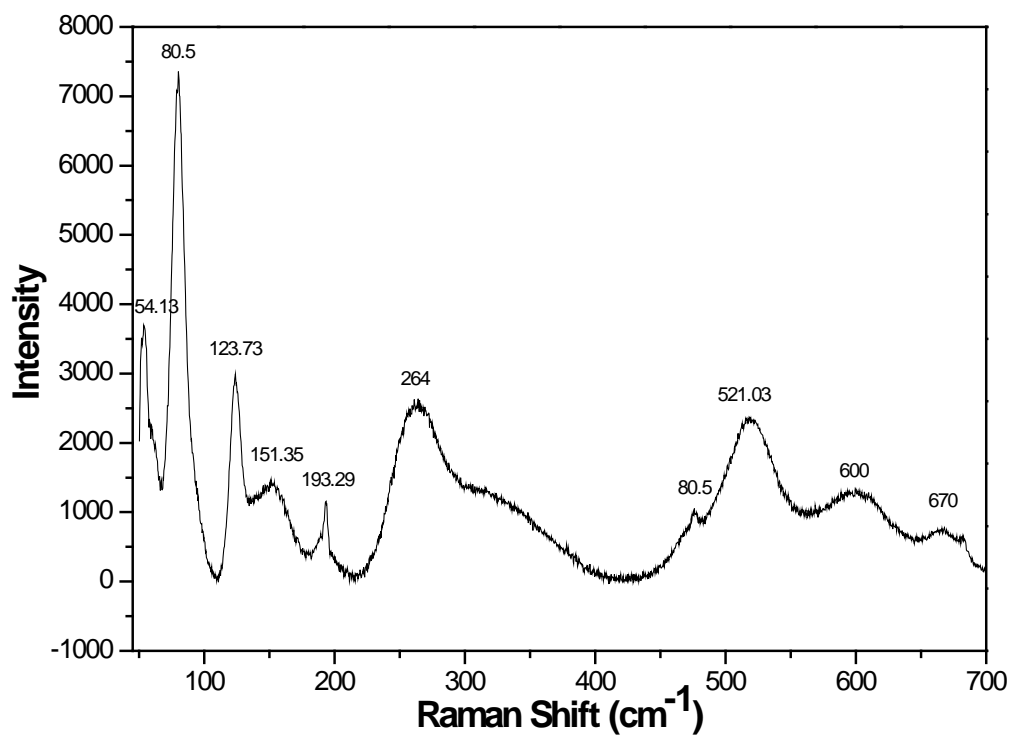


Fig. 6

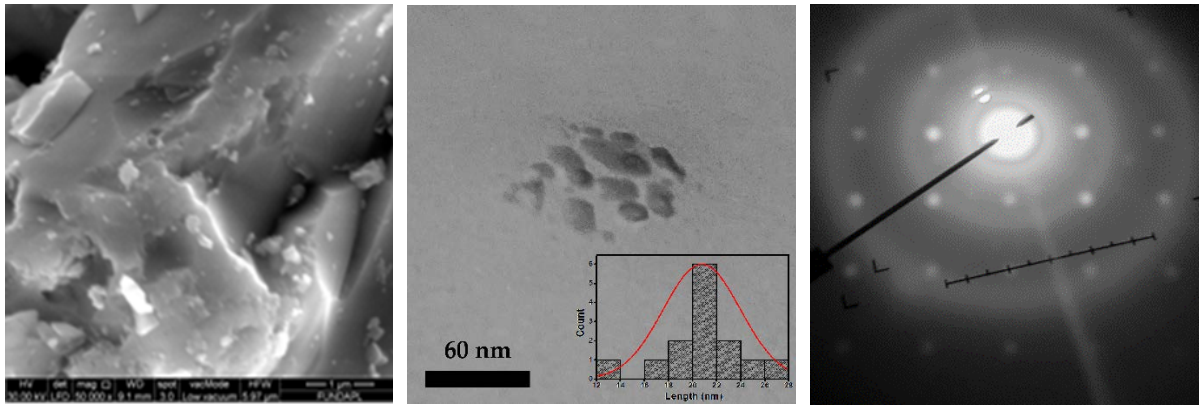
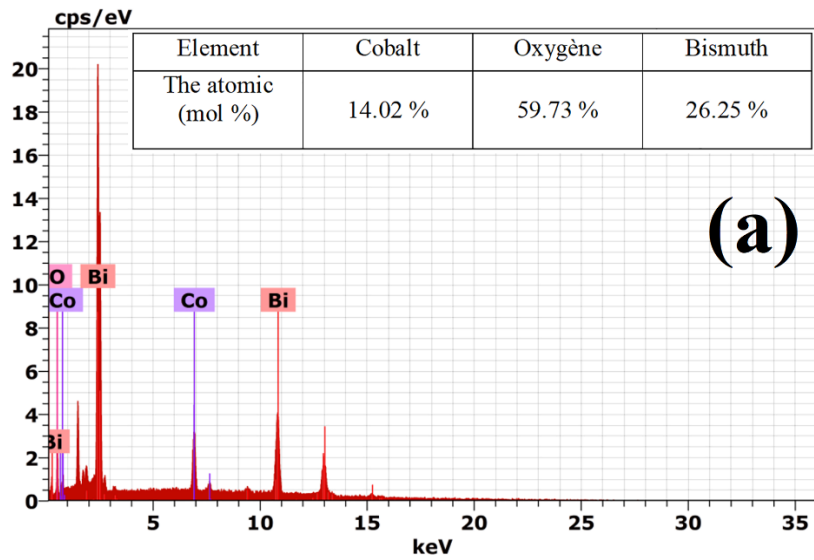
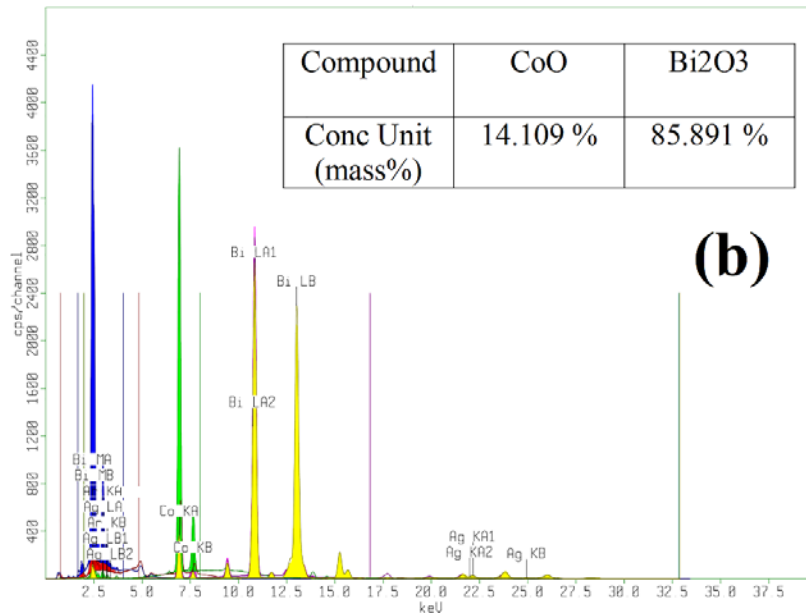


Fig. 7



(a)



(b)

Fig. 8

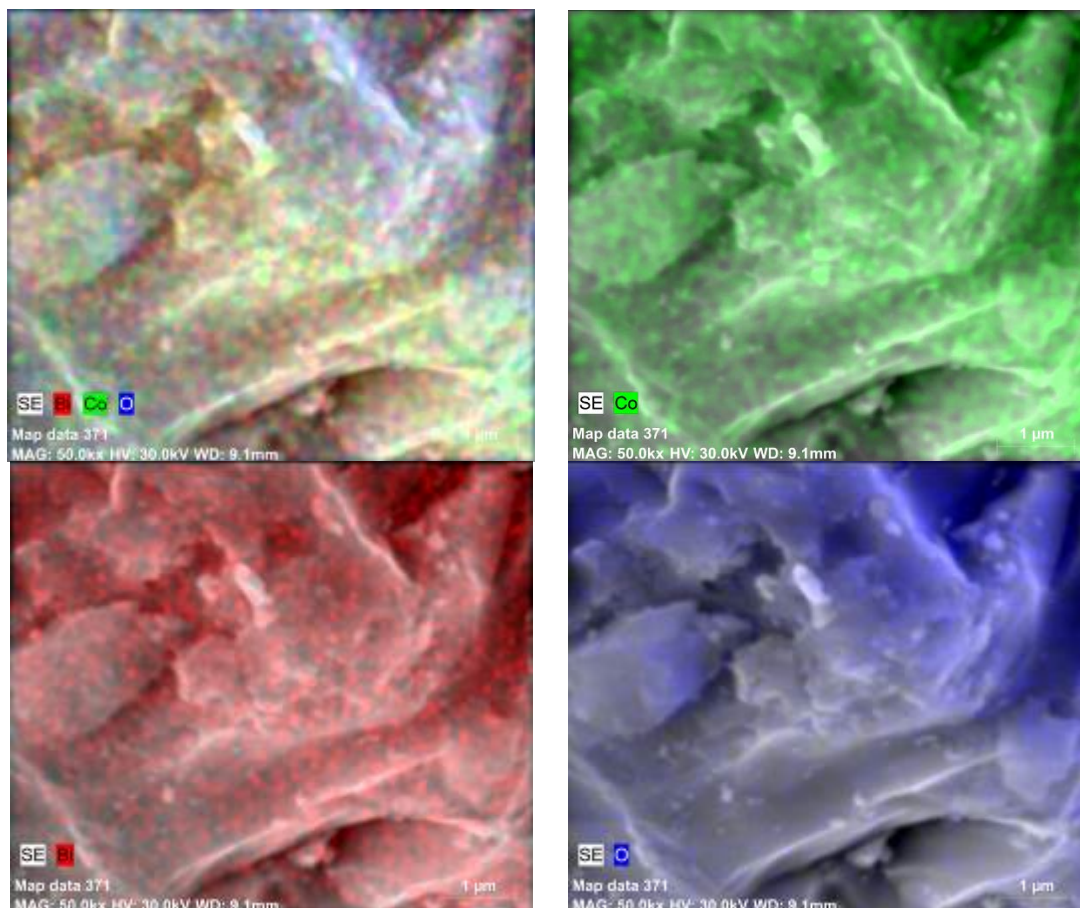


Fig. 9

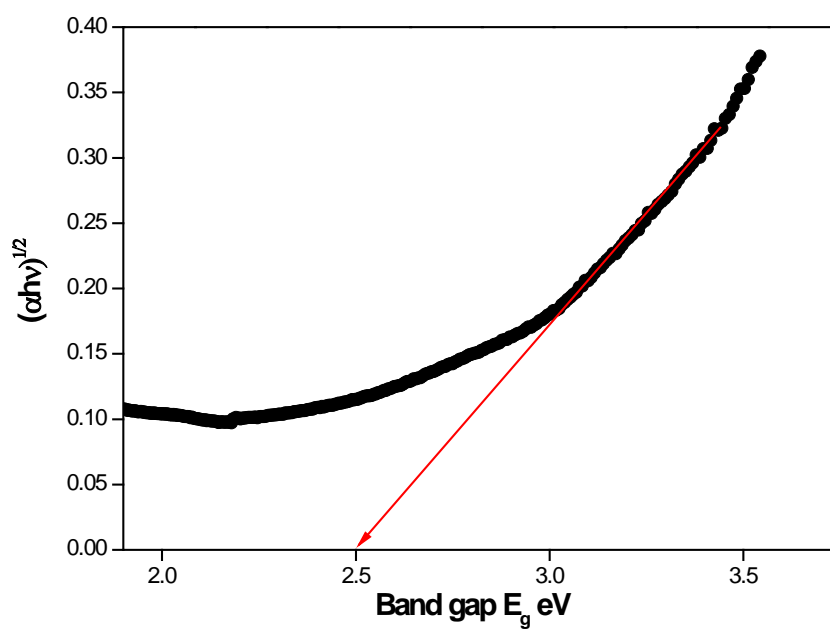


Fig. 10



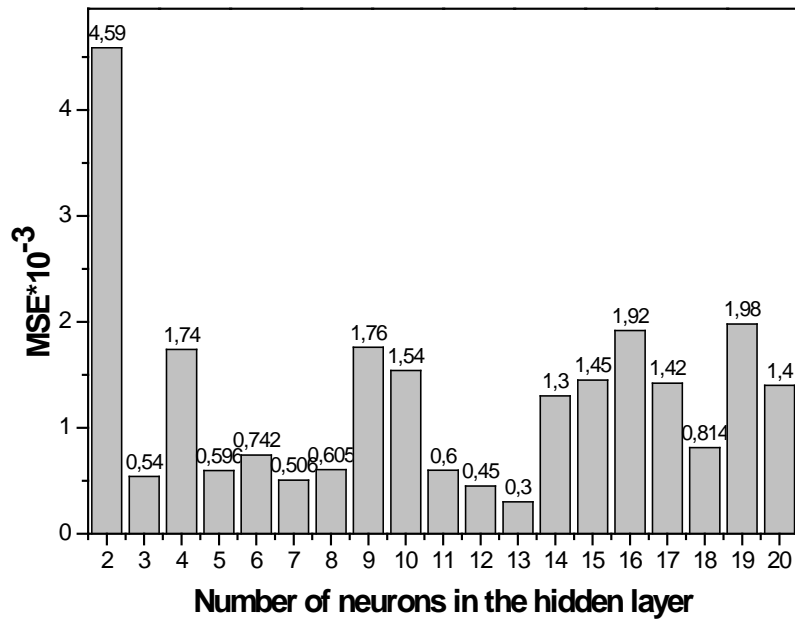


Fig. 11

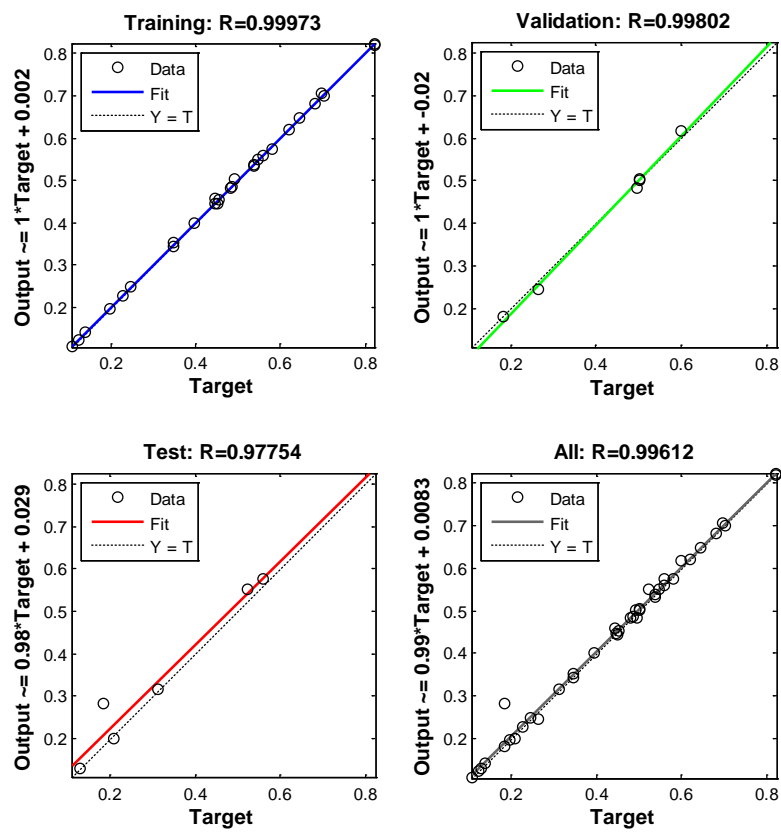


Fig. 12

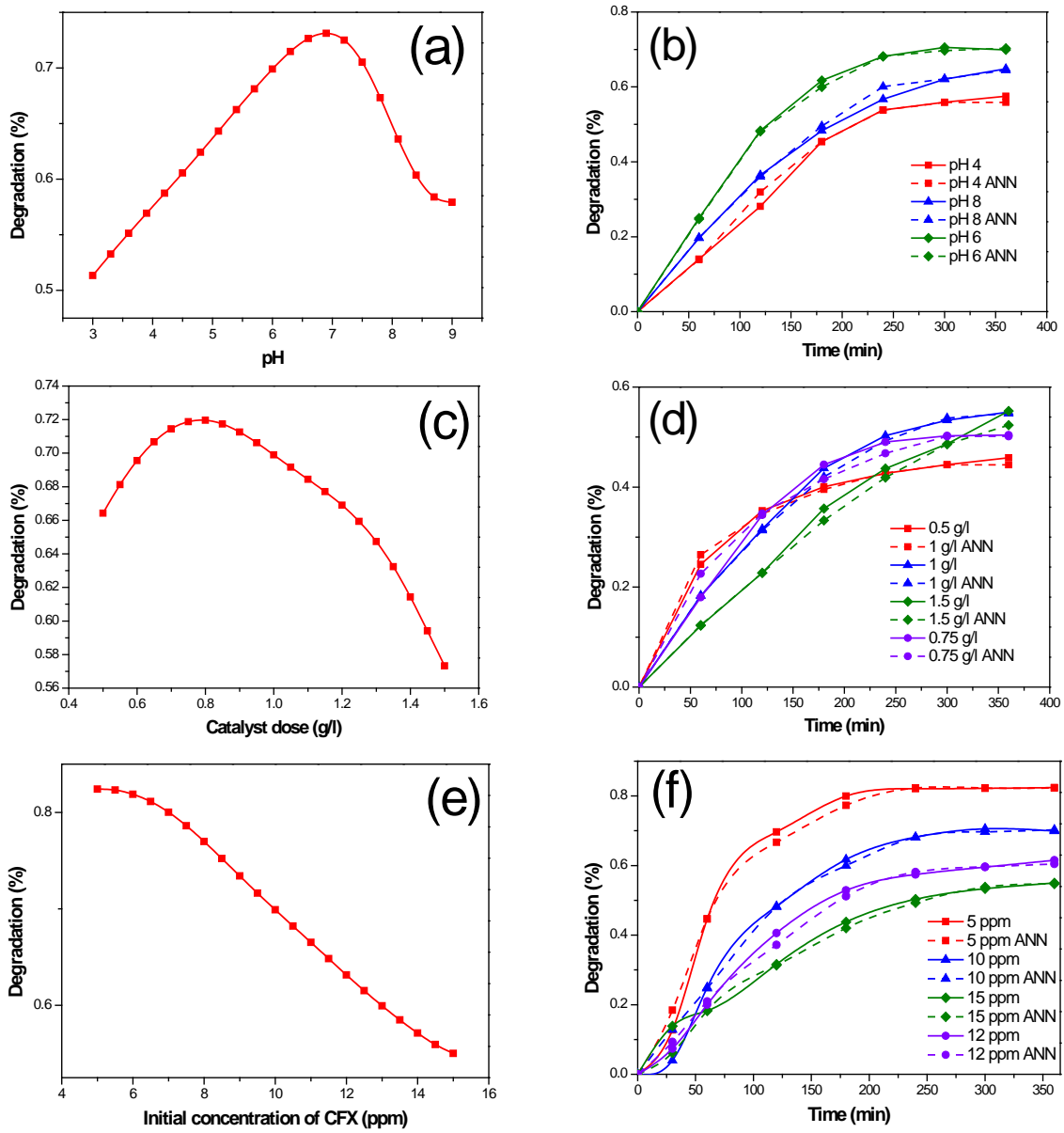


Fig. 13

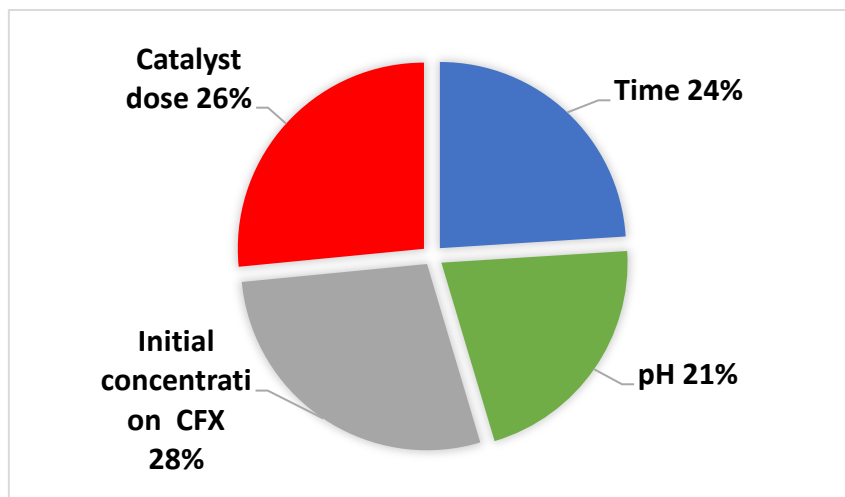


Fig. 14

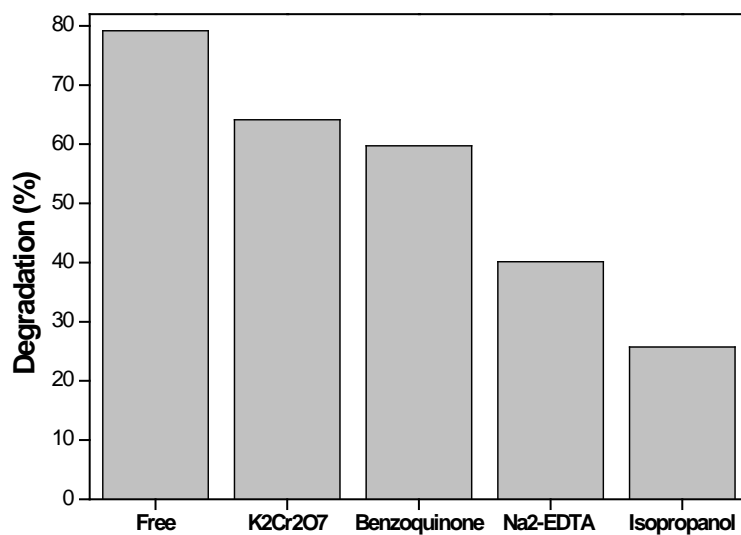


Fig. 15

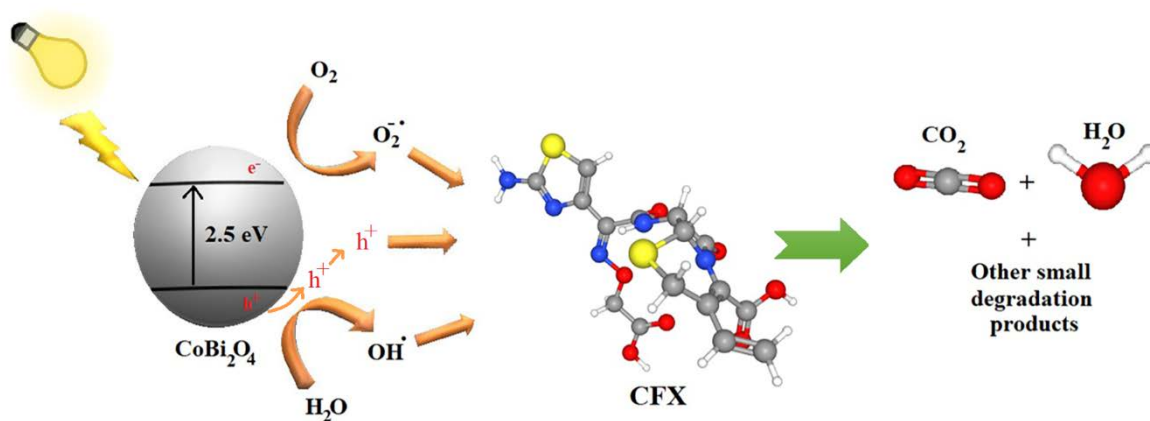


Fig. 16

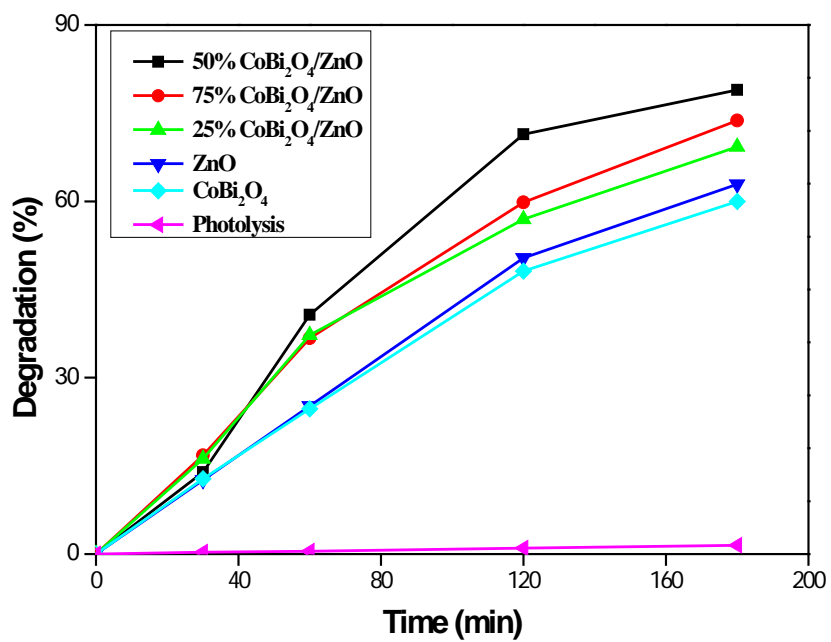


Fig. 17